Tracking a Millimetric Dual-Magnet Assembly: Toward Detecting Torsional Eye Motion

Giuseppe Bevilacqua, Valerio Biancalana, and Yordanka Dancheva

***Abstract*—Tracking eye movements with high precision is crucial for various medical and technological applications, yet detecting subtle torsional motion remains a challenge. This article presents a magnetic sensor system that accurately tracks the full six-degree-of-freedom motion (6-DoF) of a miniature dual-magnet assembly. This work leverages two (nearly) orthogonal magnetic dipoles, building upon previous results achieved with a single-dipole source. The 6-DoF tracking and the achieved level of precision may enable the detection of complex eye movements, including torsion. Moreover, the system can also track head orientation, expanding its applications in biomedical research, assistive technologies, and human–computer interaction.**

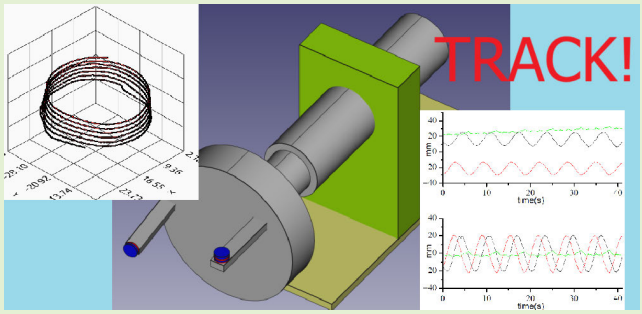

***Index Terms*— Eye motion, eye-tracking, magnetic sensor, magnetic tracker, magnetoresistor, sensor array.**

I. Introduction

TRACKING objects is crucial across numerous domains, including biological research [1], industry, security and defense [2], [3], navigation [4], and medicine. Tracking technologies and methodologies are continuously evolving.

Tracking methods based on magnetometric measurements are minimally invasive. Most materials are transparent to static magnetic fields, making magnetic tracking an occlusion-free methodology. Magnetic trackers have found various applications, including surgical [5], [6] and prosthetic [7], [8] tools, medical diagnostics [9], [10] vehicle tracking [11], biology [12], robotics [13], and security [14], [15], including covert surveillance.

Various biomedical applications exist, hinged on the achievable precision and speed. These applications encompass body part tracking (e.g., eye, tongue, hand, finger), human–machine interfaces and human–computer interaction, and virtual and augmented reality [16], [17], [18], [19].

The simplest magnetic target that can be created or modeled is a point dipole, which generates a field with a well-known expression. That field decreases with the third power of the distance and is proportional to the dipole strength [20], which in turn—for a given level of magnetization—is proportional to the volume of the source. Consequently, for a given magnetization and sensitivity, a detection system for a static dipole operates under similar conditions regardless of the scale of the problem: the targets may have sizes spanning from injectable micromagnets to large vehicles.

The rapid decrease in strength over distance allows for a fast but rough localization of a magnetic source using arrays with numerous detectors, based on the positions of those that detect a large anomaly. A quantitative analysis—e.g., based on best-fit procedures—of the field's spatial distribution enables the use of a smaller number of sensors and permits a more accurate tracking, of both the position and orientation of the source. This more advanced approach has been proposed for several delicate tasks. Among the medical ones, consider the localization on capsule endoscopes [21], [22], the study of jaw dynamics [10], [23], assessment of vestibulo-ocular reflex [24], [25], eye-tracking [26], [27], localization of implanted devices [9], and surgical tools [5].

Thanks to the superposition principle [20], magnetic tracking can be applied to localize sets of magnetic sources. While conceptually straightforward, the problem rapidly increases in complexity, as each dipolar source to be tracked comes with its degrees of freedom. Several publications report on the challenging task of simultaneously locating multiple magnetic sources [8], [28], [29], [30], [31].

The axial symmetry of the dipolar field makes the tracking of a dipole unresponsive to target rotations around the dipole direction: only five of the six degrees of freedom (6 DoFs) of a rigid body can be retrieved by marking it with a punctual dipolar source [32].

In the presence of constraints, such tracking may be enough to fully determine the pose (position and orientation) of

Received 20 March 2025; accepted 11 April 2025. Date of publication 21 April 2025; date of current version 2 June 2025. This work was supported in part by University of Siena. The associate editor coordinating the review of this article and approving it for publication was Prof. Kai Wu. *(Corresponding author: Valerio Biancalana.)*

Giuseppe Bevilacqua and Valerio Biancalana are with the DSFTA, University of Siena, 53100 Siena, Italy (e-mail: valerio.biancalana@unisi.it).

Yordanka Dancheva is with Aerospazio Tecnologie, 53040 Rapolano Teme (Siena), Italy.

Digital Object Identifier 10.1109/JSEN.2025.3561198

the rigid body. Otherwise, complete pose retrieval requires additional inputs. For instance, the position and orientation of a dipole on the eye surface would suffice to identify the eye pose, provided that the eye bulb can be modeled as a sphere whose center is known. For eye-tracking, a physiological constraint (commonly denominated Listing's law [33]) can be used to make a dipolar marker sufficient [34]. However, the use of Listing's law requires some extra information to be known beforehand, or to be determined based on dataset consistency. This involves a degree of subjectivity and a potential lack of accuracy.

Eye-tracking is often applied to identifying the gaze orientation, which (considering a patient in an erect position) is associated with rotations around the vertical axis or a horizontal transverse one. Small torsional rotations, i.e., around the gaze direction, occur as well and are of interest for medical applications. The detection of the latter by optical techniques based on pupil localization is made challenging by the axial symmetry of the analyzed feature. The localization of iris features [35], [36], [37] or artificial markers [38] has been proposed, instead. We examine the potential of magnetic tracking to detect eye rotations about arbitrary axes, thus including torsional movements.

Nonpunctual sources [28] or rigid assemblies of two (or more) dipoles allow for a complete 6-DoF determination of a rigid body's pose.

This work aims to enhance the capabilities of an eye-tracking prototype that has already been tested both in vitro [39], [40] and in vivo [24], [25] using dipolar sources, thereby overcoming the 5-DoF limitation imposed by the axial symmetry of the single-dipole field.

The task of tracking two rigidly connected dipoles is performed with a dual scope: identifying the geometrical structure of the magnetic source, and then fully determining its pose. Methods have been developed to quantify the self-consistency of the recorded data, enabling the evaluation of the 6-DoF tracking precision. This is crucial for detecting small rotations around arbitrary axes, which is essential for identifying the torsional motion of the eye bulb.

This article is organized as follows. In Section II, we describe the magnetic assembly and the detection system. In Section III, we describe the approach used to retrieve tracking data from the magnetometric ones. In Section IV, examples of tracking data and corresponding features of the assembly structure are presented in terms of trajectories and statistical distributions, as well as showing the tracks as a function of time. The system performance and its potential applications are discussed in Section V. Finally, Section VI summarizes the achievements and the analyses performed.

II. Setup

The hardware (see Fig. 1) has been thoroughly described in [39], and further details about its use as an eye tracker can be found in [24], [34], and [40]. The field detectors are distributed on a goggle-shaped frame and consist of $K = 8$ three-axial magnetoresistive sensors, providing a total of 24 simultaneous data points per measurement. The raw data are affected by offsets and unequalized gains, and thus, a preventive calibration of the sensors is necessary to convert the readings into magnetometric values (see [39] for details).

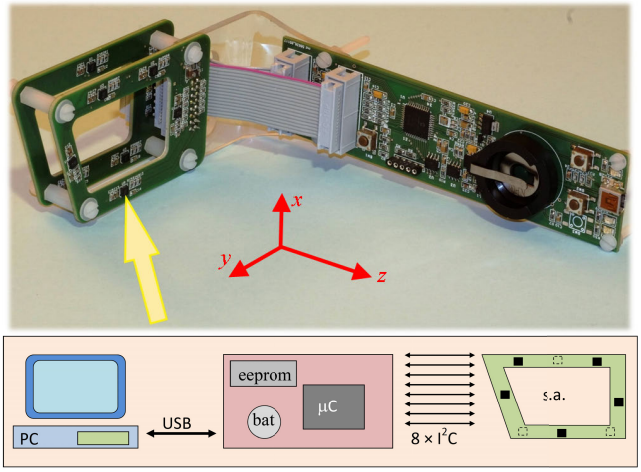

Fig. 1. Sensor contains eight three-axial magnetoresistive sensors in two sets distributed on two parallel printed circuit boards as shown in the left side of picture, where one of the sensors is indicated by the yellow arrow. An interface board (right side) enables communication between the sensors and a PC. When the goggle frame is worn for eye-tracking and the head is erect and front-oriented, $\hat{z}$ is back-directed, $\hat{x}$ is vertical, and $\hat{y}$ is transverse-horizontal. The lower schematic represents the hardware architecture, made of PC, interface board, and sensor array (s.a.). The interface board hosts a microcontroller (μC), plus a battery and memory for stand-alone used in precalibration measurements. The interface board has a USB connection with the PC, the eight sensors are set and interrogated through eight independent I^2C buses.

A microcontroller card facilitates communication between the sensor array and a personal computer (PC). The PC is used to configure the measurement parameters (rate, sensitivity, filtering) and to process, store, and analyze the readings. A USB connection ensures data transfer and powers the hardware. Data processing and tracking analysis can be done online or offline. In the first case, two independent programs run asynchronously (one to acquire and save raw data and one to elaborate and provide preliminary tracking). The elaboration program receives data through a lossy queue, enabling a quasi-real-time response, at the expense of possible disregarded data.

The current prototype uses chips (Isentek 8308 [41]) that feature three-axis anisotropic magnetoresistance sensors. These chips have built-in thermal compensation, set–reset, and analog-to-digital conversion (ADC) circuitries. The maximum data throughput rate is 200 samples per second (Sa/s) for each channel. The ADC has a 14-bit resolution, with the least significant bit corresponding to about 20 nT. Two field ranges (± 200 and ± 500 μT) can be selected, the smaller of which can be used in this application. Correspondingly, the specifications guarantee nonlinearity and hysteresis levels below 200 nT.

This type of solid-state sensor is evolving rapidly, and models based on other technologies, particularly tunnel magnetoresistors, with higher resolution and conversion rates, are currently in commerce.

The magnetic field source (see Fig. 2) is made of a rigid assembly with two small (millimetric) magnets, which are displaced by several millimeters from each other and move at centimetric distances from the sensors.

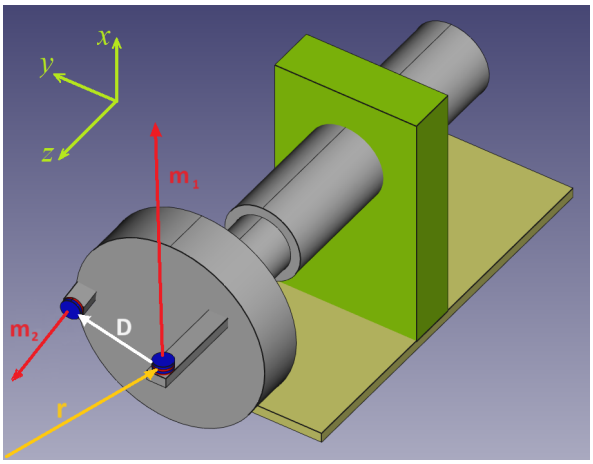

Fig. 2. Magnetic source is made of a rigid assembly (in gray) holding two magnetic dipoles (red–blue disks). The magnet size is millimetric, they are separated by $D = (19.5 \pm 0.5)$ mm (center-to-center) and rotate around an axis approximately aligned with the z-axis, at a centimetric distance from the sensors (not shown). The vectors representing the two dipoles and their relative position are not linearly dependent. The two dipoles are made by one and two Nd–Fe–B disks (each 2 mm in diameter, 0.5-mm thick), respectively. The vector $\vec{r}$ represents the position of $\vec{m}_1$ relative to the sensors' reference frame.

A dc gear motor actuates the assembly. The movement consists of a rotation around an axis approximately oriented along z. The axis is held by a normal bearing or by a threaded hole. As a result, the two magnets follow either circular or helical (1-mm pitch) trajectories, respectively, and the spatial configuration evolves periodically or quasi-periodically.

The magnet sizes are chosen so that the field they generate at the sensor positions is comparable to the Earth's magnetic field. Under these conditions, neither contribution is perturbative compared with the other, and both must (and can) be accurately determined by analyzing the magnetometric data collected.

The measurement field at the position $\vec{r}_k$ of each sensor is modeled as the superposition of a uniform (environmental) field and the fields generated by two dipoles $\vec{m}_1$ and $\vec{m}_2$, located at positions $\vec{r}$ and $\vec{r}\,' = \vec{r} + \vec{D}$, respectively, with respect to the sensors' reference frame, the patient's head reference, in the case of eye-tracking application (see Fig. 2). Here, $\vec{D}$ represents the displacement of the second dipole relative to the first one.

As will be clarified in the next, it is advisable to build assemblies in which $\vec{m}_1$, $\vec{D}$ and $\vec{m}_2$ are not linearly dependent. Instead, having the three nearly perpendicular to each other is a favorable condition. In the representation of Fig. 2, the three vectors have a nearly tangential, radial, and axial orientation, respectively. A similar configuration is shown in the pictures of the real implementation (see Fig. 3).

It is necessary to distinguish the two dipoles and to label them uniquely. In the experiments reported here, we used Nd–Fe–B disks (2-mm diameter, 0.5-mm thickness), two stacked disks as a *first dipole* and one disk as a *second dipole*. When two dipolar sources are identified, the strongest is considered to be $\vec{m}_1$ and the other $\vec{m}_2$.

In summary, the expected field on each sensor can be evaluated based on five 3-D vectors, as summarized in Table I, for a total of 15 parameters.

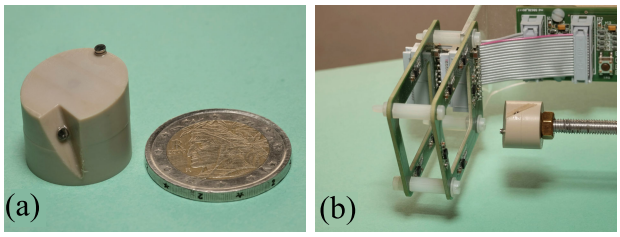

Fig. 3. Close-up picture of (a) magnetic assembly and (b) wider view showing the assembly and the sensor array.

TABLE I

DEFINITIONS OF RELEVANT QUANTITIES AND RELATED SYMBOLS (IN *Italic*, THE TRACKING PARAMETERS TO BE IDENTIFIED: EACH OF THEM COMES WITH 3 DOFS, FOR A TOTAL OF 15 DOFS). AS WILL BE SHOWN IN SECTION III, 9 DOFS RELATED TO THE TRIPLET OF VECTORS IN THE FIRST THREE LINES CAN BE REDUCED TO 3 ANGULAR DOFS, AFTER HAVING IDENTIFIED A TRIANGULAR MATRIX R REPRESENTING THOSE THREE VECTORS IN THEIR INTRINSIC REFERENCE FRAME. IN THAT CASE, THE TRACKING PROBLEM HAS ONLY 9 DOFS: $\vec{B}_{\text{GEO}}$, $\vec{r}$ AND THOSE THREE (EULER) ANGLES

symbol	description	DoF
$\vec{m}_1$	*1st dipole magnetic moment*	3
$\vec{m}_2$	*2nd dipole magnetic moment*	3
$\vec{D} = \vec{r}\,' - \vec{r}$	*position of $\vec{m}_2$ relative to $\vec{m}_1$*	3
$\vec{r}$	*absolute position of $\vec{m}_1$*	3
$\vec{r}\,'$	absolute position of $\vec{m}_2$	
$\vec{B}_{\text{geo}}$	*ambient field*	3
$\vec{r}_k$	position of the k-th sensor	

III. MODEL

As mentioned in Section II, if the field of each magnet is modeled with that of a punctual dipole, the total field on each sensor can be evaluated based on the sensor position and 15 parameters (see Table I). As the positions of the sensors are known, the (inverse) problem to be solved has 15 DoFs, at least in its first instance.

At large distances compared with D, two separate magnets produce an approximately dipolar field, with higher order multipole terms that decay faster than cubically. While we do not use this expansion, it suggests that closely located sensors can easily identify the positions of two magnets, as long as the assembly–sensor distance is not too large relative to D.

Similar to the case of single-dipole tracking performed with this apparatus [42] and with similar ones reported in the literature [8], [9], we verified that a nonlinear best-fit procedure based on the Levenberg–Marquardt (LM) algorithm serves reliably to determine the mentioned 15 parameters from the 24 magnetometric data collected. It is worth noting that other identification strategies are available, which may become essential when the number of dipoles to be tracked is large and possibly unknown and when the elaboration speed constitutes a critical parameter [31], [43].

In the case of eye-tracking based on a single dipole, we verified [42] that a large volume exists within the parameter space (much larger than all realistic configurations) where any initial guess will lead the LM algorithm to converge to the correct solution.

In the two-dipole instance, the presence of local minima is more evident and requires the initial guess to be assigned more carefully. The slow motion of the target compared with the acquisition rate renders each tracking output an excellent guess for the next best-fit procedure.

The dynamic measurements reported in this work are obtained by rotating the magnetic assembly at approximately 60 deg/s, with acquisition rates ranging from 50 to 100 Sa/s. This results in rotations of about 1 deg and submillimetric displacements between consecutive measurements.

Less favorable conditions might be encountered in vivo, in the case of saccadic movements that may occur at several hundred deg/s. In this case, a higher acquisition rate could be necessary for an adequate sampling of the eye dynamics. On the other hand, we have experimentally verified that even reducing the acquisition rate to 10 Sa/s a tracking output (therefore about 6 deg rotation between consecutive measurements) is a good guess for the next fit procedure, confirming that a 600 deg/s saccadic rotation should not produce guess issues when operating at 100 Sa/s. In conclusion, the guess criticality arises particularly when analyzing the first data of each measurement set.

A specifically implemented first-point procedure provides a practical solution to the initial guess problem. The procedure repeatedly applies the LM algorithm to the first measured dataset, using guesses randomly selected in a predetermined hypervolume of the parameter space. The guess leading to the minimum best-fit residue is selected. A few tens of attempts normally permit one to identify a guess from which the algorithm converges correctly. The data reported in this article are obtained searching the first point within a hypervolume defined as follows: spatial parameters (Cartesian components of $\vec{r}, \vec{D}$) ranging in ± 30 mm, ambient field components in ± 50 μT, and dipoles' components in ± 3 mAm^2. Guesses randomly selected in this volume lead to 10–20 minima. The good one (absolute minimum) is achieved in 10%–30% of the attempts. The others (local minima) are well-distinguishable because the corresponding residues are 1–3 orders of magnitude larger than in the case of the absolute minimum.

Even starting from suited guesses, each correct solution has a *twin* one, due to the equivalent roles played by $\vec{m}_1$ and $\vec{m}_2$. Namely, any good solution corresponds to an equivalent one obtained by swapping the indexes of the two dipoles and $\vec{r}$ with $\vec{r}'$. In other terms, the configuration $(\vec{m}_1, \vec{m}_2, \vec{D}, \vec{r}, \vec{B}_{\text{geo}})$ produces the same field as $(\vec{m}_2, \vec{m}_1, -\vec{D}, \vec{r}', \vec{B}_{\text{geo}})$. As mentioned in Section II, in this work the dipoles are labeled based on their strength: whenever the best-fit procedure outputs a solution with $m_1 < m_2$, the two vectors are swapped, and the vector $\vec{D}$ is reversed. Magnets of the same strength could be used, as well, provided that they form quite different angles with $\vec{D}$. In that case, a unique identification would be based on the comparison of those angles. After the first-point tracking, being the rotation between the $(n-1)$th and the nth acquisitions small (less than 180 deg), a reliable alternative criterion is to perform the swap whenever $\vec{D}_{n-1} \cdot \vec{D}_n < 0$.

Among the five vectors output by the LM routine (see Table I), $\vec{r}$ and $\vec{B}_{\text{geo}}$ have independent evolutions related to the translation of the magnetic source and to the movements of the sensor array, respectively. In contrast, the two dipoles and their relative position constitute a triplet nominally expected to rotate rigidly.

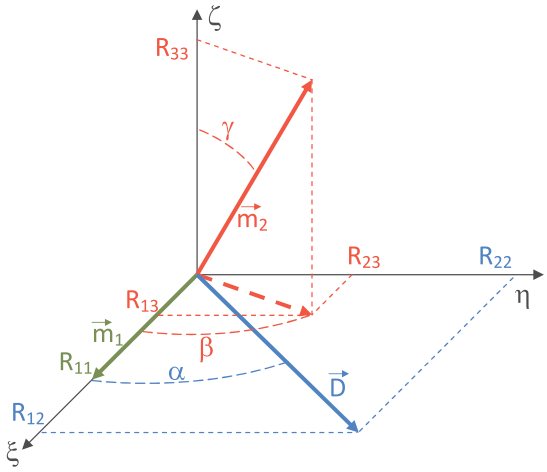

Fig. 4. In the intrinsic $\xi - \eta - \zeta$ reference frame, the three vectors that identify the assembly lay on the ξ axis, on the $\xi - \eta$ plane, and along a generic direction, respectively. Their components constitute the R elements. Three angles α, β, and γ describe their relative orientation and can be inferred from R_{ij} values.

As shown in Appendix, when the three vectors $(\vec{m}_1, \vec{D}, \vec{m}_2)$ are assembled in a matrix M, the latter can be expressed in terms of a rotated triangular matrix R, with the aid of the QR decomposition method [44]. The matrix R is made of the three vectors represented in their intrinsic $\xi - \eta - \zeta$ reference frame (see Fig. 4). A suited structure of the magnetic source (a linearly independent triplet) guarantees that M is not singular, which has relevance, as highlighted in Appendix.

The QR decomposition retrieves estimates $R^{(n)}$ of R based on each measured triplet $M^{(n)} = (\vec{m}_1, \vec{D}, \vec{m}_2)|^{(n)}$ (let n be the measurement index). Eventually, an average value $\langle R \rangle$ is obtained, which serves as an estimate of the magnetic source's structure. This structure could also be deduced from the assembly's geometry and the magnets' specifications. However, its experimental characterization is a favorite choice because it can be simpler and avoids systematic errors caused by specification uncertainties.

As said, the matrix R accounts for the geometrical details of the magnetic assembly. In particular, the angles formed by the three vectors $\vec{m}_1, \vec{D}, \vec{m}_2$ in the reference frame $\xi - \eta - \zeta$ can be expressed as

$$\begin{aligned} \alpha &= \text{atan2}(R_{22}, R_{12}) \\ \beta &= \text{atan2}(R_{23}, R_{13}) \\ \gamma &= \arccos\left(\frac{R_{33}}{\sqrt{R_{13}^2 + R_{23}^2 + R_{33}^2}}\right) \end{aligned} \tag{1}$$

using spherical co-ordinates, with the definitions provided in Fig. 4. These relationships may refer to single $R^{(n)}$ estimations or to $\langle R \rangle$.

Once the matrix R is determined, a best-fit procedure with a smaller number of parameters can be used to reanalyze

the same dataset or to elaborate new data collected with the same magnetic assembly. It is worth noting that R could be ideally evaluated from independent measurements of the magnetic dipoles and their relative position (all intended as vector quantities). However, while the distance D is easily accessible, the dipole intensity and the relative orientations of the three vectors can be hardly estimated with good accuracy.

The fitting parameters $\vec{r}$ and $\vec{B}_{\text{geo}}$ remain unchanged, while three angles (e.g., the Euler angles θ, ϕ, ψ) parameterizing a rigid rotation can be used instead of the three vectors $\vec{m}_1$, $\vec{D}$, and $\vec{m}_2$ (see Table I). To this end, the three angular parameters are used to define an orthogonal (rotation) matrix $U^{(n)} = U(\theta^{(n)}, \phi^{(n)}, \psi^{(n)})$, such that $(\vec{m}_1, \vec{D}, \vec{m}_2)|^{(n)} = U^{(n)}\langle R\rangle$. Summarizing, the number of fit parameters is reduced to 9, namely, $r_x, r_y, r_z, B_{\text{geo}-x}, B_{\text{geo}-y}, B_{\text{geo}-z}, \theta, \phi, \psi$.

Reducing the number of fitting parameters does not help shorten the computation time. The primary benefit is an improved accuracy of the best-fit results, achieved by counteracting the effects of significant covariances that arise in the case of 15-parameter best-fit.

It has been experimentally verified that it is not advisable to further reduce the number of free parameters based on the assumption that the vector $\vec{B}_{\text{geo}}$ maintains a constant modulus. The ambient field is homogeneous enough within the volume occupied by the sensor array to ignore its gradient in one measurement. However, its intensity may nonnegligibly change during measurements, because the whole system (sensor array and magnetic assembly) could move over distances much larger than the array size so that despite its weakness, ambient field gradient may play a significant role.

IV. Results

This section presents results obtained under different measurement conditions and using different best-fit procedures. The measurements are carried out under static conditions (repeated tracking of a fixed configuration) or under dynamic conditions, in which the position and orientation of the magnetic assembly change over time along predetermined trajectories. The data analysis can be based on either a 15-parameter best fit or, after the assembly structure identification, a nine-parameter one. The results can be displayed as histograms showing the distribution of the best-fit parameters, or as trajectories followed by the various vectors. It is also useful to analyze some quantities over time (i.e., versus the measurement index) because the (quasi-)periodic motion of the assembly leads to the estimation of several parameters with (quasi-)periodic systematic errors and this highlights significant covariances among spatial and magnetic variables.

The tracking performance is evaluated based on data self-consistency, i.e., the results are compared among themselves and not with independently assigned or measured quantities. Absolute accuracy and precision assessments go beyond the scope of this article.

A. 15-Parameter Fit Under Static and Dynamic Conditions

Repeated measurements under static conditions enable the quantification of the system precision, hence the minimal variation in tracking parameters that can be distinguished from the intrinsic uncertainty. Under static conditions, the estimates of tracking parameters may fluctuate due to electronic noise affecting the magnetometric data and covariances. For instance, a real variation in the ambient field due to environmental magnetic noise or rigid movements of the whole system (magnetic assembly plus sensor array) may cause an apparent variation of the magnet pose with respect to the sensors.

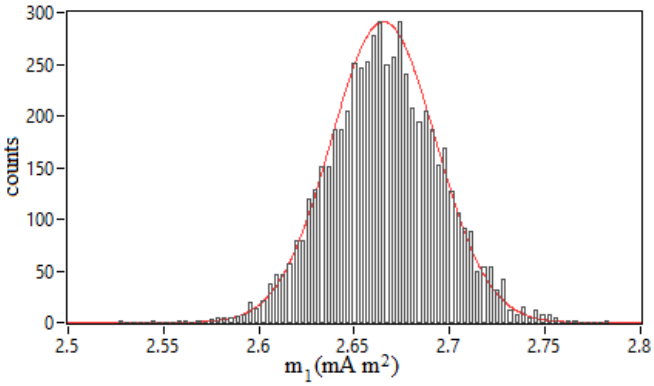

Fig. 5. Histogram of m_1 inferred from a set of static measurements.

TABLE II
Mean Value, Variance, and RSD of: Vectors' Modulus, Relative Orientation (See Fig. 4), and R_{ij} Elements

parameter	variance (σ^2)	mean (μ)	RSD ($\sigma/\lvert\mu\rvert$)
m_1 (Am^2)	8.621E-10	2.666E-3	1.101E-2
m_2 (Am^2)	5.645E-10	1.332E-3	1.783E-2
D (m)	1.471E-8	1.885E-2	6.434E-3
α (rad)	7.225E-5	-2.784E+0	3.057E-3
β (rad)	2.250E-4	2.690E+0	5.576E-3
γ (rad)	9.425E-4	1.497E+0	2.050E-2
R_{11} (Am^2)	8.621E-10	-2.666E-3	1.101E-2
R_{12} (m)	2.126E-8	6.594E-3	2.211E-2
R_{22} (m)	1.921E-8	-1.766E-2	7.850E-3
R_{13} (Am^2)	3.195E-10	4.229E-5	4.227E-1
R_{23} (Am^2)	4.985E-10	5.795E-4	3.853E-2
R_{33} (Am^2)	4.572E-10	-1.198E-3	1.784E-2

As expected, independent and small effects on a large set of sensors cause the distribution of the estimated parameters to be, at least qualitatively, normal. For example, we report in Fig. 5 a histogram of the estimated modulus of the m_1 intensity. The histogram is compared with a best-fitting Gaussian curve for a visual normality test. The experimental distributions of other parameters present quite similar profiles. Table II reports the average value, variance, and relative standard deviation (RSD) of other tracking parameters obtained from the same dataset.

Under dynamic conditions, the parameter distribution from the 15-parameter fit is broader and, in some cases, significantly deviates from a Gaussian distribution, as shown in Fig. 6. This can be ascribed to the residual gradient of the ambient field and imperfect calibration and/or nonlinearity of the sensors. Besides distorting the retrieved trajectories, the position-dependent estimates of the dipole strengths and their relative position alter their statistical distribution. An example of values obtained in dynamic conditions is reported in

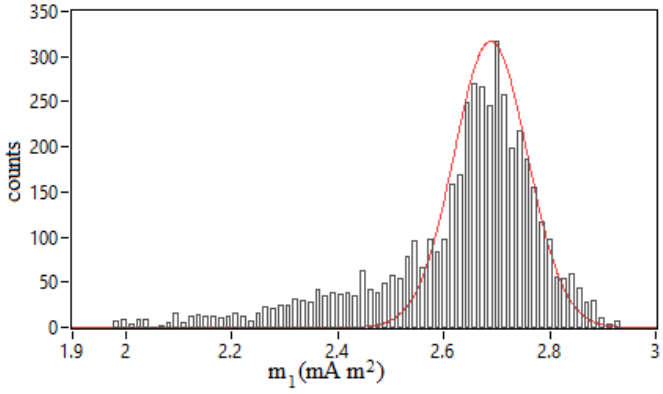

Fig. 6. Histogram of m_1 from measurements performed under dynamic conditions. Other parameters behave similarly, with asymmetric/multimodal histograms and with a larger variance compared with the static case.

TABLE III
MEAN VALUE, VARIANCE, AND RSD OF VECTOR INTENSITIES AND RELATIVE ORIENTATIONS OBTAINED FROM MEASUREMENTS PERFORMED UNDER DYNAMIC CONDITIONS

parameter	variance (σ^2)	mean (μ)	RSD (σ/μ)
m_1 (Am^2)	2.548E-8	2.628E-3	6.073E-2
m_2 (Am^2)	7.273E-9	1.265E-3	6.736E-2
D (m)	7.167E-7	2.063E-2	4.103E-2
α (rad)	4.108E-3	-2.800E+0	2.289E-2
β (rad)	4.396E-3	2.767E+0	2.396E-2
γ (rad)	3.936E-2	1.895E+0	1.000E-2
R_{11} (Am^2)	2.548E-8	-2.628E-3	6.074E-2
R_{12} (m)	2.209E-6	-7.397E-3	2.009E-1
R_{22} (m)	8.196E-7	-1.920E-2	4.716E-2
R_{13} (Am^2)	1.007E-8	-1.326E-4	7.570E-1
R_{23} (Am^2)	1.299E-8	-4.027E-4	2.829E-1
R_{33} (Am^2)	6.895E-9	-1.1835E-3	7.017E-2

Table III: these values are obtained when the assembly moves along a helicoidal trajectory, making about six turns with a 1-mm pitch at an angular speed of about 60 deg/s.

B. Nine-Parameter Fit

As said in Section III, after the 15-parameter fit has characterized the structure of the magnetic assembly (i.e., once an estimate of the matrix R is available), a nine-parameter fit can be performed to determine only quantities that vary under dynamic conditions.

The nine-parameter fit yields more regular results. By constraining certain parameters (dipole strength, relative position, and orientation), the estimates for other parameters (position and orientation of the assembly) become more precise, leading to smoother trajectories.

The accuracy depends on the estimates used to set those constraints. We typically use the median value of R elements obtained with a 15-parameter fit, either from the same dataset or from another dataset recorded under analogous conditions (same assembly performing a similar trajectory).

An assessment of the precision attained with a nine-parameter best-fit can be performed by analyzing the fluctuations of the tracking parameters observed under static conditions (differing from the 15-parameter case, under dynamic conditions, all the quantities described by the nine parameters are expected to change, preventing a precision estimate based on their standard deviation). We report in Table IV mean values and standard deviations resulting from the analysis of a dataset recorded in static condition to provide an estimate of typical precision.

TABLE IV
MEAN VALUE AND STANDARD DEVIATION OF THE POSITION, AMBIENT FIELD, AND EULER ANGLES, ESTIMATED BY NINE-PARAM BEST-FIT OF A DATASET RECORDED UNDER STATIC CONDITIONS

parameter	mean	st.dev.
r_x (mm)	9.22	0.025
r_y (mm)	22.8	0.035
r_z (mm)	28.2	0.023
$B_{\mathrm{geo-x}}$ (μT)	-42.6	0.021
$B_{\mathrm{geo-y}}$ (μT)	26.0	0.024
$B_{\mathrm{geo-z}}$ (μT)	7.78	0.056
θ (mrad)	2279	8.34
ϕ (mrad)	462	2.13
ψ (mrad)	-305	8.13

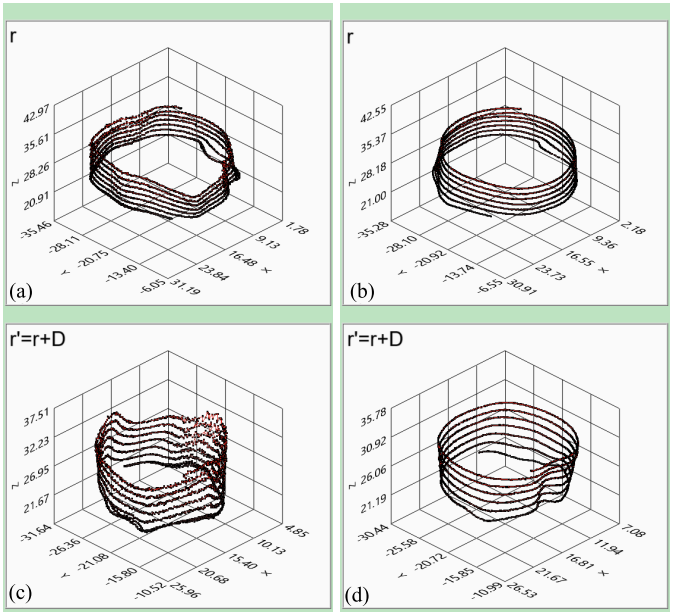

Fig. 7. Spatial trajectory of the two dipoles, as they result from (a) and (c) 15-parameter and (b) and (d) nine-parameter best-fits. The constraints set by the assignment of fixed values to R_{ij} determine a notable improvement in the precision of the trajectory. The axes are in mm.

C. Trajectories and Time-Dependencies From 15- and 9-Parameter Fits

Fig. 7 shows the spatial trajectory followed by the first dipole as reconstructed by a 15- and 9-parameter best-fit. The corresponding trajectories of the vectors $\vec{m}_1$, $\vec{m}_2$, and $\vec{D}$ are shown in Fig. 8.

Figs. 9 and 10 show the tracking results obtained with the 15-parameter fit versus time, deviations from the expected evolution (linear for r_z, constant for $\vec{B}_{\mathrm{geo}}$, sinusoidal for other parameters) can be appreciated. As already seen in the 3-D plots of the trajectories, the nine-parameter fit produces smoother results (only one example is shown).

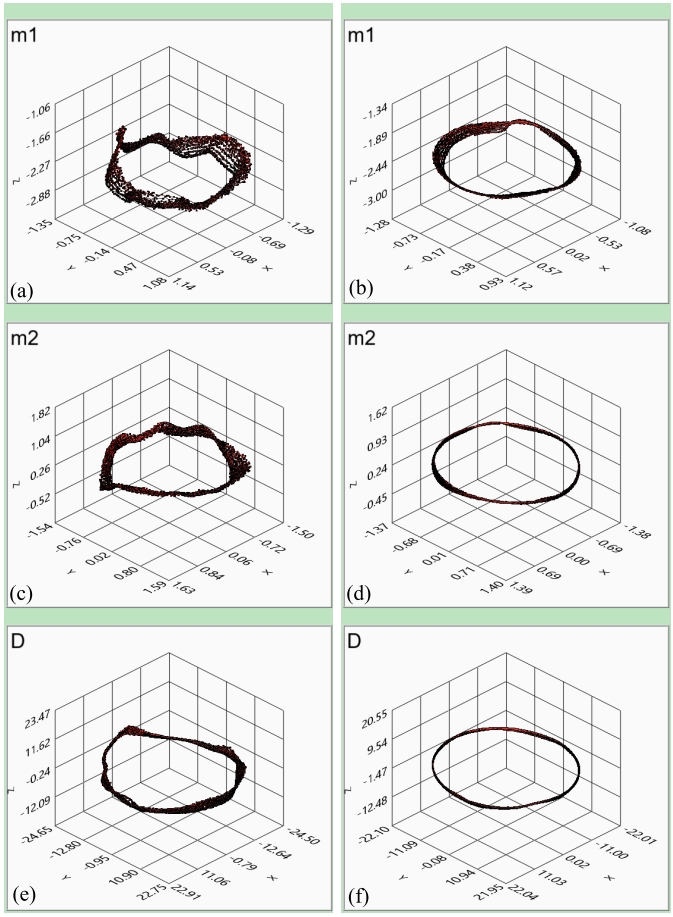

Fig. 8. Evolution of (a) and (b) $\vec{m}_1$, (c) and (d) $\vec{m}_2$, and (e) and (f) $\vec{D}$ as they result from (a), (c), and (e) 15-parameter and (b), (d), and (f) nine-parameter best fits. Note that $\vec{m}_1$ is almost aligned with the rotation axis, thus the circle size is smaller than for $\vec{m}_2$. The constant component of $\vec{m}_1$ is large and the relative uncertainties for the two dipoles are similar. A notable improvement of the precision is achieved in (b), (d), and (f) cases. Each of the three vectors has a constrained (constant) modulus, but the orientation also greatly improves. The dipoles are expressed in mAm^2, D is expressed in mm.

D. Precision Evaluation Based on SVD Decomposition

Other quantities (e.g., the R elements and the angles α, β, γ) could also be analyzed to qualitatively assess the achieved precision. However, these quantities depend on the specific assembly, and it is opportune to quantify the precision with an assembly-independent parameter.

The singular value decomposition (SVD) offers a tool to quantify the precision, as described in Appendix. Once $\langle R \rangle$ has been estimated, each measurement $M^{(n)}$ can be expressed as $M^{(n)} = B^{(n)}\langle R \rangle$, with B nominally orthogonal.

The nonorthogonality of $B^{(n)} = M^{(n)}\langle R \rangle^{-1}$ can be quantified according to 6. In Fig. 11 the quantities e and f defined in 6 (referred to the 15-parameter tracking presented in the previous figures) are plotted versus time. Both the plots present deviation from the ideal zero value, and both present peaks (more pronounced in the case of the quantity e) that coincide with spurious features appearing in the plots of Figs. 9 and 10.

V. Discussion

The results reported in Section IV demonstrate the feasibility of dual-magnet tracking based on the LM algorithm to analyze the magnetometric datasets produced by the prototypical device described in Section II.

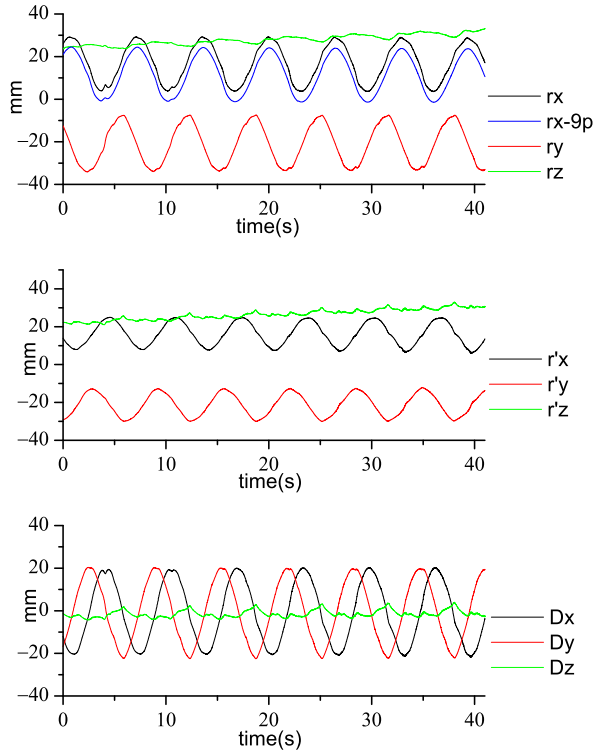

Fig. 9. Cartesian components of the absolute and relative positions of the two magnets versus time, resulting from a 15-parameter best fit. The smoother blue line corresponds to the r_x plot and is obtained with the nine-parameter fit (it is purposely displaced by 0.5 mm to avoid plot superposition).

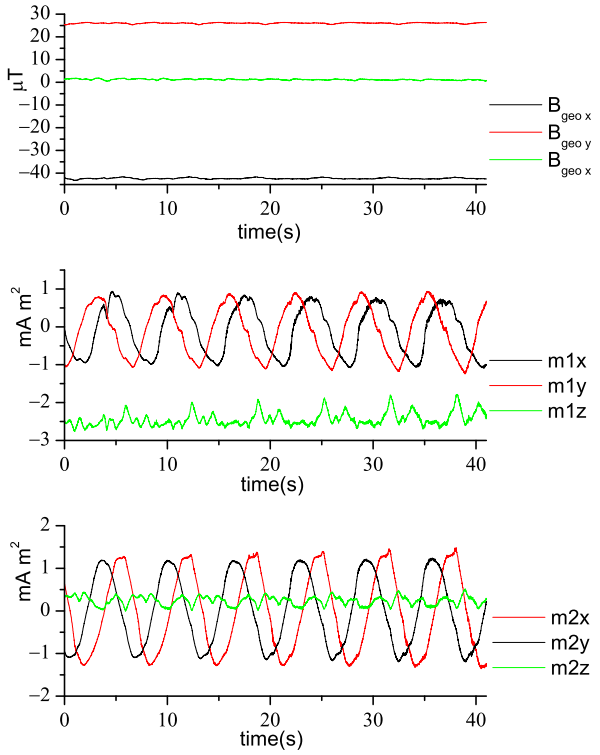

Fig. 10. Cartesian components of the environmental field and magnetic dipoles, resulting from a 15-parameter best fit. In this measurement, the sensor array was steady: minor fluctuations of $\vec{B}_{geo}$ appear concomitantly with the assembly rotation.

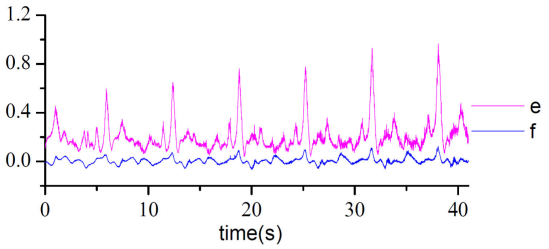

Fig. 11. SVD evaluation of the precision along the trajectory. The two plots show the quantities *e* and *f* defined by (6). Ideally, both these quantities should be zero if the pose can be represented as a pure rotation of the dual-magnet assembly. Nonzero values of *e* and *f* account for anisotropy and a nonunitary scaling factor, respectively.

The initial guess is more critical than the previously studied single-dipole tracking. Still, the method developed to assign a suited guess proved to be effective and reliable despite its simplicity. The data elaboration rate is slower than that of the single dipole case. Typical values are 50 tracking outputs per second, using an ordinary PC. This value is suited for online data analysis using a lossy queue, while it demands an offline analysis for a complete elaboration with full time-resolution.

The performance observed under dynamic conditions is worse than under static ones, making the accuracy level worse than the precision one. Several imperfections may originate trajectory distortions and other position-dependent errors, due to unequalized response of the sensors. The latter can be due to field inhomogeneities affecting the precalibration procedure [39] and to sensor response variations, e.g., due to thermal drifts or elapsing time. We have verified that field gradients typically present in the room do not cause evident degradation. Magnetized materials nearby, such as steel chairs and iron furniture, can generate spurious field gradients. Therefore, it is advisable to take precautions to minimize interference from such objects. As known, gradient decays with the fourth power of distance, and this makes it crucial to select nonferromagnetic devices and connectors for the circuitry in the sensors' proximity, as they would be detrimental despite their small size. According to the specifications, the sensors operate well within their linear response range. However, minor nonlinearities in their response may still contribute to trajectory distortions and crosstalk between various parameters, such as the sensor frame's orientation and the magnetic source's pose.

It is worth noting that the results obtained under dynamic conditions must be considered as a *typical*, but cannot be used to strictly quantify the system performance. The calibration imperfections of the diverse sensors may introduce biases in the position and orientation estimates, depending on the specific configuration. This may result in trajectory distortion and position-dependent errors in the orientation estimates. The same may occur as a consequence of an imperfectly homogeneous background field. The parameters' distributions depend on diverse contingent conditions, such as the specific trajectory assigned to the magnetic assembly, the sensors' calibration accuracy, and the ambient field's local inhomogeneities. Crosstalking among diverse fitting parameters may cause large variations in some (positional and/or angular) parameters to appear as minor changes in some others. In particular, large reorientations of the gaze cause important displacement and rotation of the assembly, which might spuriously result in an apparent torsion. For instance, the orientation of $\vec{m}_1$ inferred from Fig. 8(a) and (b) has evident bias errors that vary along the trajectory. Measurements aimed at detecting torsional movements should be performed under conditions of small gaze reorientation, i.e., would be mainly limited by the precision and not by the accuracy of the torsional angle estimate.

As already discussed in the case of single-dipole tracking [24], the passage from in vitro to in vivo measurements might introduce additional uncertainty sources, such as those due to slippage of the assembly on the eye bulb or the sensor frame on the head, further artifacts can be caused by eye-blinking that can displace the contact lens.

Both in the case of 15- and 9-parameter fits, small displacements of the target result in pretty close tracking outputs, while large displacements cause significant variation in the systematic errors with consequent distortion of the reconstructed trajectories, particularly in the 15-parameter case. This feature indicates that the precision level exceeds the accuracy confirming the high level of reproducibility observed under static conditions (see Table IV).

In some applications, precision and reproducibility play a role more important than accuracy. For instance, consider detecting small torsional motion, which is challenging for all the competing eye-tracking methodologies. In such an application, one needs to detect small variations of the eye pose (particularly rotations around the visual axis), while it is unessential to identify the object observed or measure large reorientations of the gaze. Consequently, the limiting factors are those identified in the static-condition performance.

From the variances of the angular quantities reported in Table II, uncertainties ranging from 0.5 deg (for α) to 1.7 deg (for γ) are estimated. Estimating the accuracy from the corresponding data reported in Table III (i.e., measured under dynamic conditions) leads to about ten times worse results. It is worth noting that we are here dealing with the angles that describe the structure of the magnetic assembly and not its orientation in space.

The nine-parameter fit provides a clearer indication of the angular uncertainty, as it outputs the Euler angles of the rotated rigid frame rather than the angles among the $\vec{m}_1, \vec{D}, \vec{m}_2$ vectors. The same data measured under static conditions that produce the results in Table II, with a 15-parameter best-fit, when analyzed with a 9-parameter fit provide Euler angles whose standard deviations are between 0.13 deg and 0.45 deg. In concomitance with the smoother and more consistent spatial trajectories [see Figs. 7(b) and (d) and 8(b), (d), and (f)], the nine-parameter fit improves the angular precision.

For eye-tracking purposes, the magnetic assembly (with the three vectors about mutually perpendicular) could be implemented using magnets with axial and diametrical magnetization, as schematized in Fig. 12.

Concerning the determination of the absolute gaze direction, the procedure would require a calibration step, in which the subject observes an assigned target. Let $\vec{u}^{(0)}$ be a unit vector directed from the eye to the target and let $M^{(0)}$ be $(\vec{m}_1, \vec{D}, \vec{m}_2)$

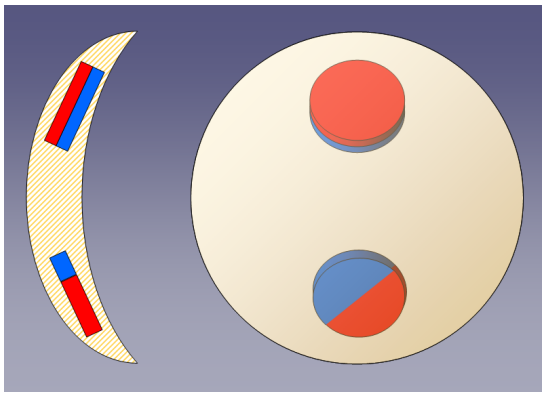

Fig. 12. Aiming at eye-tracking, the examined assembly can be implemented in a contact lens using two disk-shaped magnets with axial and diametral magnetization, respectively.

measured in that condition (an averaging can be performed to determine a $\langle M^{(0)}\rangle$, for improved accuracy).

Now assuming that $M^{(n)}$ is the result at the generic measurement, it is expected that $M^{(n)} = A\langle M^{(0)}\rangle$, with $A = M^{(n)}\langle M^{(0)}\rangle^{-1}$ nominally orthogonal: $\vec{u}^{(n)} = A\vec{u}^{(0)}$ will (approximately) be a unit vector oriented along the current (nth) gaze direction.

The simultaneous tracking of $\vec{B}_{\text{geo}}$ can be used to produce an absolute gaze tracking, i.e., relative to the ambient field and not to the sensor array.

VI. Conclusion

We have presented a system and methodology for tacking two rigidly assembled magnetic dipoles. This system is specifically designed for application to eye-tracking. Unlike the single-dipole case, this system allows full localization of the tracked rigid body (the patient's ocular bulb), identifying its three spatial and three angular degrees of freedom relative to the sensor array, while also measuring the ambient field. The latter enables the determination of two out of the three degrees of freedom that describe the absolute orientation of the sensor array (the patient's head) in the laboratory frame. Details of the system performance analyses based on data self-consistency have been provided.

Angular uncertainty is influenced by measurement conditions and the best-fit procedure used to analyze magnetometric data. With the considered setup—which has the advantage of being operated in vitro and the disadvantage of not being fully optimized in terms of the spatial distribution of the sensors—we have achieved angular uncertainties better than half a degree.

Appendix

We make use of QR decomposition of 3×3 matrices. It is worth recalling that any real square matrix A may be decomposed as $A = QR$ where Q is an orthogonal matrix, and R is an upper triangular matrix.

Provided that $\det A \neq 0$, the factorization is unique if the diagonal elements of R must have preassigned signs, e.g., all positive [44]. Concerning the physical meaning of Q, orthogonal 3×3 matrices describe the composition of rotations and/or reflections in the usual 3-D Euclidean space.

Specifically, when $\det Q = +1$, Q describes the composition of rotations and of an even number of reflections, which can be more simply considered as a unique rotation.

In the case of 15-parameter fit (see Section III) the LM routine outputs $\vec{r}$, $\vec{B}_{\text{geo}}$, $\vec{m}_1$, $\vec{D}$, and $\vec{m}_2$. The three latter are expected to rotate rigidly and the QR decomposition is applied to the matrix having them three in the columns

$$QR = M = \begin{pmatrix} m_{1x} & D_x & m_{2x} \\ m_{1y} & D_y & m_{2y} \\ m_{1z} & D_z & m_{2z} \end{pmatrix}. \tag{2}$$

For the sake of unicity.

1) It is first required that all the diagonal elements of R are positive.
2) If it is found $\det Q = -1$, then R and Q are replaced by CR and QC, with

$$C = \begin{pmatrix} 1 & 0 & 0 \\ 0 & 1 & 0 \\ 0 & 0 & -1 \end{pmatrix} \tag{3}$$

(this case occurs when $\vec{m}_1$, $\vec{D}$, and $\vec{m}_2$ constitute a right-handed triplet).

Now $\det Q = +1$ and the Q matrix describes a rotation from the system $x - y - z$ to a system $\xi - \eta - \zeta$ where $\vec{m}_1$ is oriented along ξ, $\vec{D}$ lays on the $\xi - \eta$ plane, $\vec{m}_2$ is generically oriented

$$R = \begin{pmatrix} m_{1\xi} & D_\xi & m_{2\xi} \\ 0 & D_\eta & m_{2\eta} \\ 0 & 0 & m_{2\zeta} \end{pmatrix} \tag{4}$$

with $m_{1\xi}, D_\eta > 0$. The left/right-handed orientation of the triplet is preserved.

This process is repeated for each measurement in succession. Let n be the measurement index. We consider the $M^{(n)}$ fit output along with the corresponding $R^{(n)}$ triangular matrices. Ideally, the columns of the $R^{(n)}$ matrices represent repeated estimates of the rigid triplet, expressed in its $\xi - \eta - \zeta$ system. These matrices can then be averaged to estimate the structure of the magnetic assembly, denoted as $\langle R\rangle$.

As an alternative, each $R^{(n)}$ can be analyzed to determine the relative orientation of $\vec{m}_1$, $\vec{D}$, and $\vec{m}_2$ and their moduli [see (1)], aiming to determine a mean value of R from the averaged vectors. The two estimates may differ due to the nonlinear operations involved. However, we experimentally verified that the two methods lead to very close estimates (within 1%, typically), and we opted for the first one, for its simpler implementation.

Once a reliable estimation $\langle R\rangle$ of the triplet is available, the best-fit procedure can be performed with a reduced number of free parameters. In fact, besides $\vec{r}$, $\vec{B}_{\text{geo}}$ vectors, only three angles—such as the Euler angles—are necessary to define a rotation matrix $U^{(n)}$ such that $U^{(n)}\langle R\rangle$ is the current configuration of the magnetic source assembly.

Another well-known matrix factorization is the so-called SVD, based on which a matrix A can be expressed as

$$A = U\Sigma V^{\mathrm{T}} \tag{5}$$

in which U and V are orthogonal matrices and Σ is a diagonal one with positive elements. In the general case, if A is an $m \times n$ matrix, U is $m \times m$, Σ is $m \times n$, and V is $n \times n$. In our case $n = m = 3$, i.e., we deal with 3×3 matrices only.

Consider the case that $M^{(n)}$ and $M^{(p)}$ contain the vectors $\vec{m}_1, \vec{D}$, and $\vec{m}_2$ estimated in two instances. Let $M^{(n)} = A^{(n,p)}M^{(p)}$ and hence $A = M^{(n)}(M^{(p)})^{-1}$. In the case of a rigid rotation, A is ideally an orthogonal matrix and its SVD decomposition would lead to $\Sigma = \mathbb{I}$, being $A = UV^{\mathrm{T}}$.

In real cases, due to experimental uncertainties affecting $M^{(n)}$ and $M^{(p)}$, $A^{(n,p)}$ is only approximately orthogonal and $\|E\| = \|\Sigma - \mathbb{I}\|$ can be used to evaluate the discrepancy between A and an exactly orthogonal transformation.

Alternatively, the discrepancy can be quantified by

$$e = \frac{\lambda_1}{\lambda_3} - 1, \quad \text{and}$$
$$f = \sqrt{\frac{\lambda_1^2 + \lambda_2^2 + \lambda_3^2}{3}} - 1 \tag{6}$$

being λ_i the eigenvalues of Σ (the singular values of A) in descending order, with e and f accounting for the anisotropy and the scaling factor, respectively.

Instead of two independent measurements, $M^{(n)}$ and $M^{(p)}$, the SVD analysis may involve $M^{(n)}$ and $\langle R \rangle$: this is the case of (e, f) quantities reported in Section IV.

REFERENCES

[1] A. Cavagna et al., "The STARFLAG handbook on collective animal behaviour: 1. Empirical methods," *Animal Behaviour*, vol. 76, no. 1, pp. 217–236, Jul. 2008.

[2] S. Abba, A. M. Bizi, J.-A. Lee, S. Bakouri, and M. L. Crespo, "Real-time object detection, tracking, and monitoring framework for security surveillance systems," *Heliyon*, vol. 10, no. 15, Aug. 2024, Art. no. e34922.

[3] C. Deans, L. Marmugi, and F. Renzoni, "Through-barrier electromagnetic imaging with an atomic magnetometer," *Opt. Exp.*, vol. 25, no. 15, pp. 17911–17917, 2017.

[4] J. Cao, H. Zhang, L. Jin, J. Lv, G. Hou, and C. Zhang, "A review of object tracking methods: From general field to autonomous vehicles," *Neurocomputing*, vol. 585, Jun. 2024, Art. no. 127635.

[5] C. Di Natali, M. Beccani, and P. Valdastri, "Real-time pose detection for magnetic medical devices," *IEEE Trans. Magn.*, vol. 49, no. 7, pp. 3524–3527, Jul. 2013.

[6] Y. Zhang, W. W. Clark, B. Tillman, Y. J. Chun, S. Liu, and S. K. Cho, "A system to track stent location in the human body by fusing magnetometer and accelerometer measurements," *Sensors*, vol. 23, no. 10, p. 4887, May 2023.

[7] M. Gherardini, A. Mannini, and C. Cipriani, "Optimal spatial sensor design for magnetic tracking in a myokinetic control interface," *Comput. Methods Programs Biomed.*, vol. 211, Nov. 2021, Art. no. 106407.

[8] V. Ianniciello, M. Gherardini, and C. Cipriani, "Transcutaneous magnet localizer for a self-contained myokinetic prosthetic hand," *IEEE Trans. Biomed. Eng.*, vol. 71, no. 3, pp. 1068–1075, Mar. 2024.

[9] J. T. Sherman, J. K. Lubkert, R. S. Popovic, and M. R. DiSilvestro, "Characterization of a novel magnetic tracking system," *IEEE Trans. Magn.*, vol. 43, no. 6, pp. 2725–2727, Jun. 2007.

[10] M. Jucevičius, R. Ožiūnas, and D. Jegelevičius, "Wireless intraoral jaw motion tracker performance evaluation and demonstration of operation in vitro and in vivo," *IEEE Sensors J.*, vol. 24, no. 1, pp. 822–829, Jan. 2024.

[11] N. Wahlström and F. Gustafsson, "Magnetometer modeling and validation for tracking metallic targets," *IEEE Trans. Signal Process.*, vol. 62, no. 3, pp. 545–556, Feb. 2014.

[12] J. J. Jun, A. Longtin, and L. Maler, "Real-time localization of moving dipole sources for tracking multiple free-swimming weakly electric fish," *PLoS ONE*, vol. 8, no. 6, Jun. 2013, Art. no. e66596.

[13] T. D. Than, G. Alici, H. Zhou, and W. Li, "A review of localization systems for robotic endoscopic capsules," *IEEE Trans. Biomed. Eng.*, vol. 59, no. 9, pp. 2387–2399, Sep. 2012.

[14] M. Sun, R. Hodgskin-Brown, M. E. Davies, I. K. Proudler, and J. R. Hopgood, "Adaptive kernel Kalman filter for magnetic anomaly detection-based metallic target tracking," in *Proc. Sensor Signal Process. Defence Conf. (SSPD)*, Sep. 2023, pp. 1–5.

[15] R. Sithiravel, B. Balaji, B. Nelson, M. K. McDonald, R. Tharmarasa, and T. Kirubarajan, "Airborne maritime surveillance using magnetic anomaly detection signature," *IEEE Trans. Aerosp. Electron. Syst.*, vol. 56, no. 5, pp. 3476–3490, Oct. 2020.

[16] H. L. Payne and J. L. Raymond, "Magnetic eye tracking in mice," *ELife*, vol. 6, p. 29222, Sep. 2017.

[17] V.-M. Saarinen and V. Jousmäki, "Eye tracking in MEG," *Attention, Perception, Psychophys.*, vol. 87, pp. 238–244, Jan. 2024.

[18] Y. Shi et al., "Eye tracking and eye expression decoding based on transparent, flexible and ultra-persistent electrostatic interface," *Nature Commun.*, vol. 14, no. 1, p. 3315, Jun. 2023.

[19] K. Lenard, X. Liang, A. Tanwear, and H. Heidari, "Eye tracking simulation for a magnetic-based contact lens system," in *Proc. 27th IEEE Int. Conf. Electron., Circuits Syst. (ICECS)*, Nov. 2020, pp. 1–2.

[20] J. D. Jackson, *Classical Electrodynamics-Magnetostatics, Faraday's Law, Quasi-static Fields*. New York, NY, USA: Wiley, 1999, ch. 5.

[21] C. Hu, M. Q.-H. Meng, and M. Mandal, "Efficient magnetic localization and orientation technique for capsule endoscopy," *Int. J. Inf. Acquisition*, vol. 2, no. 1, pp. 23–36, Mar. 2005.

[22] W. Weitschies, J. Wedemeyer, R. Stehr, and L. Trahms, "Magnetic markers as a noninvasive tool to monitor gastrointestinal transit," *IEEE Trans. Biomed. Eng.*, vol. 41, no. 2, pp. 192–195, Feb. 1994.

[23] M. Jucevičius, R. Ožiūnas, G. Narvydas, and D. Jegelevičius, "Permanent magnet tracking method resistant to background magnetic field for assessing jaw movement in wearable devices," *Sensors*, vol. 22, no. 3, p. 971, Jan. 2022.

[24] G. Bevilacqua et al., "A wearable wireless magnetic eye-tracker, in-vitro and in-vivo tests," *IEEE Trans. Biomed. Eng.*, vol. 70, no. 12, pp. 3373–3380, Dec. 2023.

[25] A. Donniacuo, F. Viberti, M. Carucci, V. Biancalana, L. Bellizzi, and M. Mandalà, "Development of a magnetoresistive-based wearable eye-tracking system for oculomotor assessment in neurological and otoneurological research—Preliminary in vivo tests," *Brain Sci.*, vol. 13, no. 10, p. 1439, Oct. 2023.

[26] A. Tanwear et al., "Spintronic sensors based on magnetic tunnel junctions for wireless eye movement gesture control," *IEEE Trans. Biomed. Circuits Syst.*, vol. 14, no. 6, pp. 1299–1310, Dec. 2020.

[27] A. S. Almansouri, "Tracking eye movement using a composite magnet," *IEEE Trans. Magn.*, vol. 58, no. 4, pp. 1–5, Apr. 2022.

[28] W. Yang, C. Hu, M. Q.-H. Meng, S. Song, and H. Dai, "A six-dimensional magnetic localization algorithm for a rectangular magnet objective based on a particle swarm optimizer," *IEEE Trans. Mag.*, vol. 45, no. 8, pp. 3092–3099, Aug. 2009.

[29] W. Yang, C. Hu, M. Li, M. Q.-H. Meng, and S. Song, "A new tracking system for three magnetic objectives," *IEEE Trans. Magn.*, vol. 46, no. 12, pp. 4023–4029, Dec. 2010.

[30] S. Song, C. Hu, and M. Q.-H. Meng, "Multiple objects positioning and identification method based on magnetic localization system," *IEEE Trans. Magn.*, vol. 52, no. 10, pp. 1–4, Oct. 2016.

[31] L. Miao, T. Zhang, C. Zuo, Z. Chen, X. Yang, and J. Ouyang, "A rapid localization method based on super resolution magnetic array information for unknown number magnetic sources," *Sensors*, vol. 24, no. 10, p. 3226, May 2024.

[32] V. Schlageter, P.-A. Besse, R. S. Popovic, and P. Kucera, "Tracking system with five degrees of freedom using a 2D-array of Hall sensors and a permanent magnet," *Sens. Actuators A, Phys.*, vol. 92, nos. 1, pp. 37–42, Aug. 2001.

[33] A. M. Wong, "Listing's law: Clinical significance and implications for neural control," *Surv. Ophthalmol.*, vol. 49, no. 6, pp. 563–575, Nov. 2004.

[34] V. Biancalana and P. Chessa, "A non-inductive magnetic eye-tracker: From dipole tracking to gaze retrieval," *Instruments*, vol. 7, no. 1, p. 8, Feb. 2023.

[35] E. Groen, J. E. Bos, P. F. M. Nacken, and B. de Graaf, "Determination of ocular torsion by means of automatic pattern recognition," *IEEE Trans. Biomed. Eng.*, vol. 43, no. 5, pp. 471–479, May 1996.

[36] J. K. Y. Ong and T. Haslwanter, "Measuring torsional eye movements by tracking stable iris features," *J. Neurosci. Methods*, vol. 192, no. 2, pp. 261–267, Oct. 2010.
[37] N. Jin, S. Mavromatis, J. Sequeira, and S. Curcio, "A robust method of eye torsion measurement for medical applications," *Information*, vol. 11, no. 9, p. 408, Aug. 2020.
[38] A. A. Migliaccio, H. G. MacDougall, L. B. Minor, and C. C. D. Santina, "Inexpensive system for real-time 3-dimensional video-oculography using a fluorescent marker array," *J. Neurosci. Methods*, vol. 143, no. 2, pp. 141–150, Apr. 2005.
[39] V. Biancalana, R. Cecchi, P. Chessa, G. Bevilacqua, Y. Dancheva, and A. Vigilante, "Fast, cheap, and scalable magnetic tracker with an array of magnetoresistors," *Instruments*, vol. 5, no. 1, p. 3, Dec. 2020.
[40] L. Bellizzi et al., "An innovative eye-tracker: Main features and demonstrative tests," *Rev. Scientific Instrum.*, vol. 93, no. 3, Mar. 2022, Art. no. 035006.
[41] *3D Magnetometer—Brief Datasheet*, Standard IST 8308, iSentek, 2017.
[42] V. Biancalana et al., "Validation of a fast and accurate magnetic tracker operating in the environmental field," *Instruments*, vol. 5, no. 1, p. 11, Mar. 2021.
[43] H. Ge, S. Song, J. Wang, and M. Q.-H. Meng, "Multi-magnet tracking method using extended Kalman filter," in *Proc. IEEE Sensors*, Oct. 2021, pp. 1–4.
[44] G. H. Golub and C. F. Van Loan, *Matrix Computations*. Baltimore, MD, USA: The Johns Hopkins Univ. Press, 2013, ch. 5.

Giuseppe Bevilacqua is a Researcher with the DSFTA, University of Siena, Siena, Italy. He is interested in modeling phenomena related to condensed matter problems such as quantum optics and phase transitions. His research interests include theoretical nature and spans a range of different phenomena from quantum optics, solid state physics, phase transitions in liquid crystals, and developing applications of quantum optical phenomena to atomic magnetometry.

Valerio Biancalana is an Associate Professor with the DSFTA, University of Siena, Siena, Italy. He is an Experimental Physicist with experience in laser–plasma interaction, laser-cooling, laser spectroscopy, and development of optical magnetometers. Applied magnetometry is among his current interests, also with diverse kinds of sensors. He matured experience in application of highly sensitive magnetometers to experiments of biomagnetism, ultralow-field NMR, and detection of weakly magnetized materials.

Yordanka Dancheva is a Researcher with Aerospazio Tecnologie, Siena, Italy, and an Experimental Physicist specialized in laser spectroscopy and the development of optical magnetometers. She has extensive experience in applying highly sensitive magnetometers to a range of fields, including biomagnetism, ultralow-field NMR, and the detection of weakly magnetized materials. Another key area of her work—closely linked to laser spectroscopy—is the development and application of non-intrusive plasma diagnostics, particularly in plasmas generated by electric propulsion systems.